

# Ultr sensitive Sniff-Cam for Biofluorometric-Imaging of Breath Ethanol Caused by Metabolism of Intestinal Flora

Kenta Iitani,<sup>†,‡,§,||</sup> Koji Toma,<sup>||</sup> Takahiro Arakawa,<sup>||</sup> and Kohji Mitsubayashi<sup>\*,§,||</sup>

<sup>†</sup>Postdoctoral Research Fellow PD, Japan Society for the Promotion of Science, 5-3-1 Kojimachi, Chiyoda-ku, Tokyo 102-0083, Japan

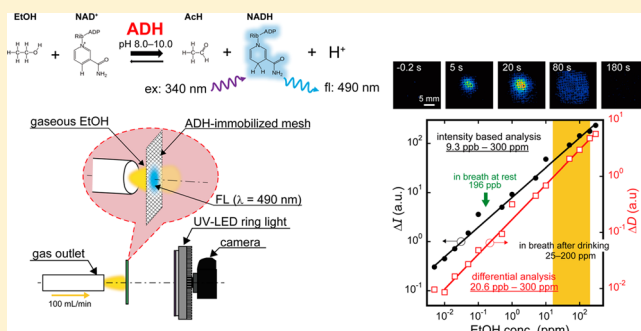
<sup>‡</sup>Department of Life Science and Medical Bioscience, Graduate School of Advanced Science and Engineering, Waseda University (TWIns), 2-2 Wakamatsu-cho, Shinjuku-ku, Tokyo 162-8480, Japan

<sup>§</sup>Graduate School of Medical and Dental Sciences, Tokyo Medical and Dental University, 1-5-45 Yushima, Bunkyo-ku, Tokyo 113-8510, Japan

<sup>||</sup>Department of Biomedical Devices and Instrumentation, Institute of Biomaterials and Bioengineering, Tokyo Medical and Dental University, 2-3-10 Kanda-Surugadai, Chiyoda-ku, Tokyo 101-0062, Japan

## Supporting Information

**ABSTRACT:** We developed a gas-imaging system (sniff-cam) for gaseous ethanol (EtOH) with improved sensitivity. The sniff-cam was applied to measure the extremely low concentration distribution of breath EtOH without the consumption of alcohol, which is related to the activity of the oral or gut bacterial flora. A ring-type ultraviolet-light-emitting diode was mounted around a camera lens as an excitation light source, which enabled simultaneous excitation and imaging of the fluorescence. In the EtOH sniff-cam, a nicotinamide adenine dinucleotide (NAD)-dependent alcohol dehydrogenase (ADH) was used to catalyze the redox reaction between EtOH and the oxidized form of NAD (NAD<sup>+</sup>). Upon application of gaseous EtOH to the ADH-immobilized mesh that was soaked in an NAD<sup>+</sup> solution and placed in front of the camera, NADH was produced through an ADH-mediated reaction. NADH expresses fluorescence at an emission wavelength of 490 nm and excitation wavelength of 340 nm. Thus, the concentration distribution of EtOH was visualized by measuring the distribution of the fluorescence light intensity from NADH on the ADH-immobilized mesh surface. First, a comparison of image analysis methods based on the red–green–blue color (RGB) images and the optimization of the buffer pH and NAD<sup>+</sup> solution concentration was performed. The new sniff-cam showed a 25-fold greater sensitivity and broader dynamic range (20.6–300000 ppb) in comparison to those of the previously fabricated sniff-cam. Finally, we measured the concentration distribution of breath EtOH without alcohol consumption using the improved sniff-cam and obtained a value of  $116.2 \pm 35.7$  ppb ( $n = 10$ ).



## 1. INTRODUCTION

In the ancient world, before analytical techniques for volatile organic compounds (VOCs) were developed,<sup>1</sup> both the smell of exhaled breath and body odor were used to aid in disease diagnosis.<sup>2</sup> VOCs, however, are contained in the exhaled breath and skin secretions of not only those with diseases but also those of healthy people.<sup>3,4</sup> Additionally, the types of VOCs secreted by a human vary as a result of many factors, including smoking habits,<sup>5</sup> sex,<sup>6</sup> and body mass index.<sup>7</sup> Disease and metabolic conditions can also generate specific VOCs and induce a noticeable change in the concentrations of these compounds. However, this change in concentration is usually very small, and in many cases, human olfaction cannot perceive it. Therefore, various analytical techniques have been developed that allow us to elucidate the relationship between VOCs and some diseases, such as Parkinson's disease,

Alzheimer's disease,<sup>8,9</sup> diabetes mellitus,<sup>10</sup> skin cancer,<sup>11,12</sup> lung cancer,<sup>13,14</sup> and renal disease.<sup>15</sup> Turner et al. examined the relationship between lifestyle and breath ethanol (EtOH) and acetaldehyde (AcH) levels by measuring their concentrations over a long period using selected-ion flow-tube mass spectrometry (SIFT-MS).<sup>16</sup> According to their paper, there is a significant difference between the concentrations of EtOH in the breath of people who consumed a sugary drink or food within 2 h of the testing (323 ppb) and of those who did not (115 ppb). Conversely, no significant difference was observed in the concentrations of AcH under the same conditions. It has been suggested that this escalation of EtOH concentration in

Received: December 19, 2018

Accepted: June 17, 2019

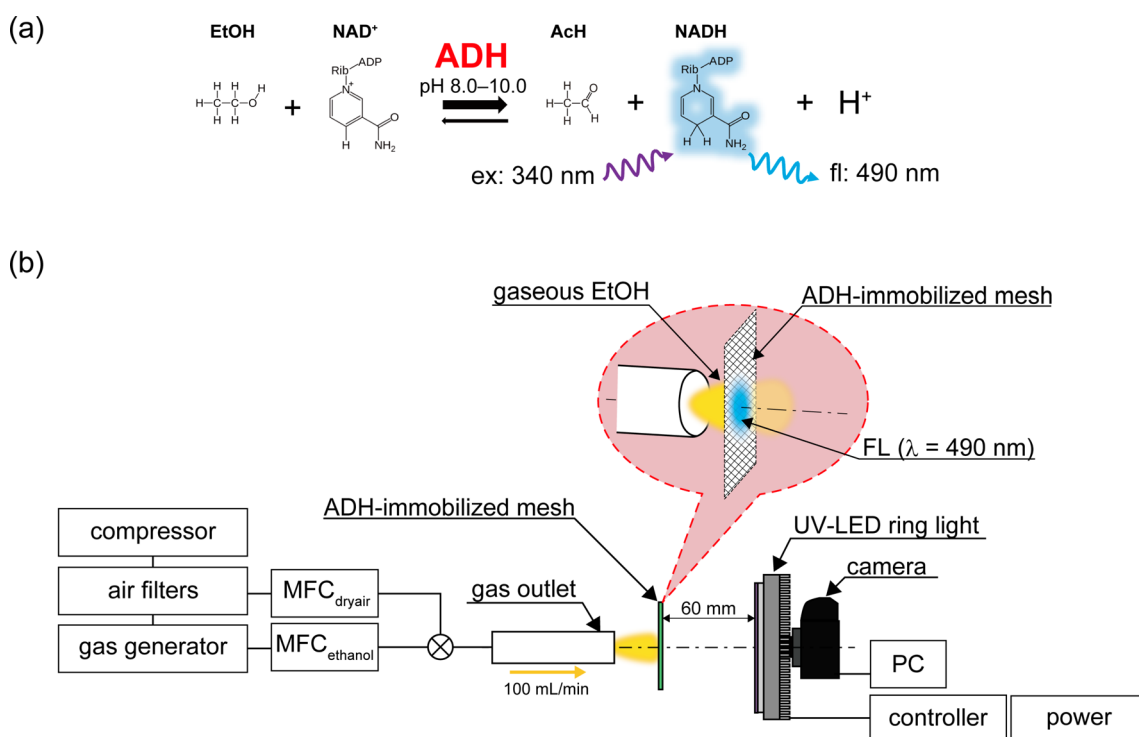


**Figure 1.** (a) Principle of gaseous EtOH detection via a biofluorometric imaging technique based on the ADH-mediated enzymatic reaction. (b) Experimental setup of the EtOH sniff-cam with a UV-LED ring light.

breath is caused by fermentation in the oral cavity or gut bacterial flora.<sup>17</sup> The relationship between glucose and EtOH is also of interest. Research has shown that the simultaneous measurement of breath VOCs such as acetone, which is a biomarker for lipid metabolism, and breath EtOH can be used to predict glucose concentration.<sup>18–20</sup> Currently, the most common breath and skin gas analysis method involves a large analytical instrument such as that for gas chromatography–mass spectrometry, which provides an advantage in the identification of VOCs in a complex mixture, as well as high sensitivity.<sup>21</sup>

On the other hand, these analytical systems are usually bulky and expensive and require professional skill and long times to analyze a sample. As such, small and cost-effective chemical gas sensors based on a metal oxide,<sup>22</sup> quartz crystal microbalance,<sup>23</sup> and localized surface plasmon resonance<sup>24</sup> have been developed. However, these systems face challenges in terms of selectivity when they are applied to breath or gas released from skin (skin gas). Enzymatic biosensors seem suitable for the analysis of breath and skin gas because they possess high selectivity based on substrate specificity.<sup>25,26</sup>

Recently, imaging techniques of chemicals including VOCs are advancing. For example, Liu's group published papers about smartphone-based biochemical sensing and imaging of VOCs.<sup>27–29</sup> Also, Hou's group reported a highly selective optoelectronic nose based on surface plasmon imaging for VOCs.<sup>30,31</sup> Biochemical analysis with imaging seems suitable for medical fields because of it can analyze a large number of samples and a nonprofessional person can recognize the results with the naked eye.

Previously, fiber-optic biochemical gas sensors (bio-sniffers) that exploit nicotinamide adenine dinucleotide (NAD) dependent enzymes to achieve high selectivity were developed.<sup>32,33</sup> These bio-sniffers could measure acetone and

isopropyl alcohol levels, which are markers of lipid metabolism and potential biomarkers of lung cancer, respectively, with high sensitivity (the limit of quantification (LOQ) was 20 ppb for acetone and 1 ppb for isopropyl alcohol). Monitoring of the concentration of skin EtOH gas was also achieved using bio-sniffers that utilize alcohol dehydrogenase (ADH), which has a wide dynamic range against EtOH (25–128000 ppb).<sup>34</sup> This measurement technique was used to develop a gas visualization system (sniff-cam).<sup>35</sup> The sniff-cam allowed the visualization of the spatial distribution of EtOH emanating from the skin after alcohol consumption. However, the quantitative properties of the sniff-cam (500–200000 ppb) did not come close to those of the EtOH bio-sniffer. Thus, it is difficult to image the distribution of breath and skin gas EtOH without the consumption of alcohol.

In this study, we constructed a new optical system consisting of a ultraviolet (UV) light emitting diode (LED) ring light and a red–green–blue (RGB) camera and then improved the sensitivity of the EtOH sniff-cam by a novel image-analysis method that can effectively measure the fluorescence of the reduced form of NAD<sup>+</sup> (NADH) by utilizing an RGB color image. First, the concentration distribution of gaseous EtOH was transduced to a fluorescence intensity distribution by utilizing an enzyme mesh. This mesh was prepared by ADH immobilization within a cotton mesh substrate, and the fluorescence was captured by the camera. We then compared several image analysis methods using the RGB image. Subsequently, the reaction conditions of the ADH, including the pH of the buffer solution and concentration of the coenzyme solution, were optimized and the characteristics of the improved sniff-cam were evaluated. Finally, using the highly sensitive sniff-cam, we visualized the breath EtOH concentration obtained from healthy subjects who had not consumed alcohol or food.

## 2. MATERIALS AND METHODS

**2.1. Materials and Reagents.** ADH (E.C. 1.1.1.1, from *Saccharomyces cerevisiae*, 369 units/mg solid, A7011) was purchased from Sigma-Aldrich. A cotton mesh substrate (100% cotton, 1 mm thickness, 1 mm interval) was obtained from Ohki Healthcare Holdings. We used the cotton mesh as the substrate for the ADH-immobilized mesh because it showed little autofluorescence at a wavelength of 490 nm under exposure to UV light at a wavelength of 340 nm, a suitable characteristic for the required fluorescence measurement. Glutaraldehyde (GA, 25%, 079-00533, Wako) and bovine serum albumin (BSA, 306-13383, Wako) were respectively used as a cross-linker and an enzyme-stabilizing reagent for ADH immobilization. Oxidized nicotinamide adenine dinucleotide ( $\text{NAD}^+$ , 44057000), which was used as a coenzyme for the ADH-mediated EtOH oxidation, was purchased from Oriental Yeast. The following reagents were used for buffer preparation: acetic acid (99.7%, 017-00256, Wako), sodium acetate (98.5%, 192-01075, Wako), potassium dihydrogen phosphate (99.5%, 169-04245, Wako), disodium hydrogen phosphate (99.0%, 197-02865, Wako), trisodium phosphate dodecahydrate (98.0%, 191-082885, Wako), 2-amino-2-hydroxymethyl-1,3-propanediol (99.0%, 013-16385, Wako), hydrochloric acid (35%, 083-3485, Wako), sodium hydrogen carbonate (99.5%, 191-01305, Wako), sodium carbonate (99.8%, 199-01585, Wako), sodium hydroxide (97.0%, 37187-08, Kanto Chemical), and potassium chloride (99.5%, 163-03545, Wako). All buffers were prepared using ultrapure water that was generated by a purification system (Purelab Flex, Elga). A standard sample of gaseous EtOH was generated by a standard gas generator (Parmater PB-1B-2, Gastec) with a diffusion tube (No. 3200, Gastec) that was filled with an EtOH solution (99.5%, 14033-00, Kanto Chemical).

**2.2. Construction of the EtOH Sniff-Cam Using a Ring-Type UV-LED.** Figure 1a shows the principle of gaseous EtOH detection utilized by the sniff-cam. ADH catalyzes the redox reaction between EtOH and  $\text{NAD}^+$ , which produces AcH and NADH. Since NADH shows autofluorescence via excitation at a wavelength of 340 nm and subsequent fluorescence at a wavelength of 490 nm, we determined the EtOH concentration by measuring the fluorescence intensity of NADH. An ADH-immobilized mesh, which was used to facilitate the aforementioned redox reaction of EtOH, was prepared by the following process. First, the ADH solution was prepared by dissolving lyophilized ADH powder (135 units, 0.365 mg) and BSA (0.56 mg) in 112.5  $\mu\text{L}$  of a phosphate buffer solution (PB, pH 8.0, 0.1 M). Second, the ADH solution was cast on the cotton mesh substrate (15 mm  $\times$  15 mm) homogeneously and left for 1 h in a dark place at 4  $^\circ\text{C}$ . Third, a GA solution (2.5%, v/v, 18  $\mu\text{L}$ ) prepared with PB (pH 7.0, 0.1 M) was spread on the cotton mesh substrate in order to cross-link the ADH, and the mesh was stored for 1.5 h in a dark place at 4  $^\circ\text{C}$ . Finally, the excess of the non-cross-linked ADH was removed by rinsing with PB (pH 8.0, 0.1 M).

Figure 1b displays the experimental setup of the EtOH sniff-cam. The EtOH sniff-cam was composed of an RGB camera (ILCE-7S, Sony), a custom-made ring-type UV-LED light (DOWA), two bandpass filters (BPFs), and the ADH-immobilized mesh. The ring-type UV-LED excitation light source, which consisted of 40 UV-LED chips (providing light emission at a wavelength of  $340 \pm 5$  nm, DOWA), was used to obtain homogeneous excitation on the plane of the ADH-

immobilized mesh. The light source was mounted around a lens of the camera using a through hole with a diameter of 75 mm. A custom-made BPF for the excitation light ( $\text{BPF}_{\text{ex}}$  with a wavelength of  $340 \pm 42.5$  nm and dimensions of 100 mm width, 100 mm height, and 2.5 mm thickness; Hoya Candeo Optonics) also had a through hole with a diameter of 75 mm in the center; this BPF was mounted on the light source. A BPF for the fluorescence light ( $\text{BPF}_{\text{fl}}$  with a wavelength of  $492 \pm 10$  nm and diameter of 50 mm, Edmund) was mounted in front of the camera lens. The ring-type UV-LED light source was connected to a stabilized direct current power supply (KX-100H, Takasago) and driven by applying a current of 0.320 A. The camera was connected to a computer for the purpose of control. Video was taken using RGB coloring with dimensions of 1920 pixels  $\times$  1080 pixels at 24 frames per second.

**2.3. Image Analysis Method Based on the RGB Imaging of NADH Fluorescence.** Visualization of standard gaseous EtOH was demonstrated by the developed system. First, the ADH-immobilized mesh was wetted with 80  $\mu\text{L}$  of  $\text{NAD}^+$  solution (10 mM) that had been prepared using a Tris-HCl buffer (0.1 M of Tris at pH 9.0). Changes in the fluorescence intensity of the ADH-immobilized mesh were then captured by a camera, while 100 ppm of standard gaseous EtOH at a flow rate of 100 mL/min was applied. Standard gaseous EtOH was generated by a diffusion tube method, which is one of the standard methods used to obtain standard gas via dry and clean air. This air was fed to a standard gas generator through an air filter (3001-17201, GL-Science) and a silica-gel air dryer (3001-17111, GL-Science) from an air compressor (SLP-15EBD, Anest Iwata). An EtOH gas visualization experiment was performed through the following process. First, we captured images including the background 100 s after application of dry and clean air to the  $\text{NAD}^+$ -wetted ADH-immobilized mesh. After 20 s of recording, the applied gas was changed to standard EtOH and application was maintained for 20 s. The applied gas was then immediately changed back to dry and clean air, and image capturing was stopped 170 s after this change. After that, the mean fluorescence intensity of a region of interest (ROI, 120 pixels  $\times$  120 pixels) was set around the center of each frame of the captured video and was calculated by an image processing program.

A previous system used a camera that had an equipped monochrome image sensor. The system developed here, however, utilized a color camera that could capture RGB images. Hence, an image analysis method based on the RGB images was developed and compared with the previous method. An RGB image was composited using three independent eight-bit grayscale images composed of red, green, and blue channels. A novel bicolor image method allowed the creation of a composite image generated by the simple addition of the green and blue images. Evaluation of five methods of image analysis, namely, a single-channel analysis of the red, green, and blue channels, a grayscale image analysis that was generated on the basis of eq 1, and analysis of a bicolor image that was generated on the basis of eq 2, was performed to compare the respective signal and noise (S/N) ratios.

$$\begin{aligned} \text{gray images} &= 0.299 \times \text{red} + 0.587 \times \text{green} \\ &\quad + 0.114 \times \text{blue} \end{aligned} \quad (1)$$

$$\text{bicolor images} = \text{green} + \text{blue} \quad (2)$$



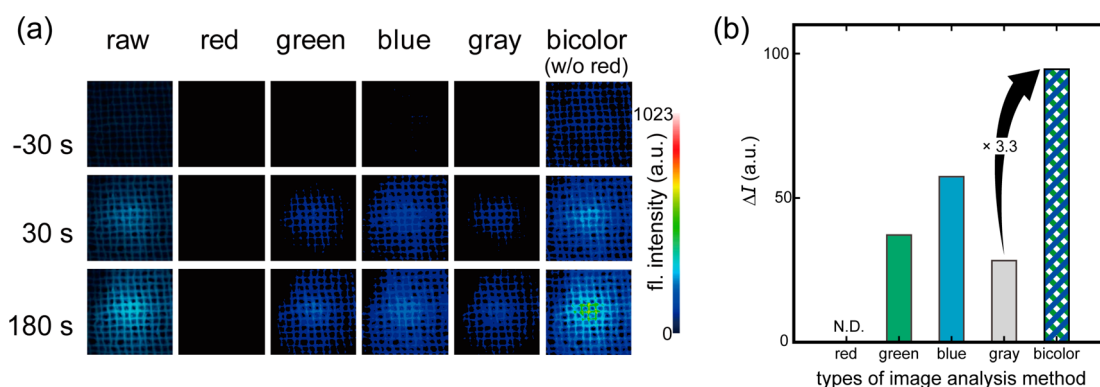


**Figure 2.** (a) Fluorescence images at  $-30$ ,  $30$ , and  $180$  s after applying of gaseous EtOH at  $100$  ppm. The methods used from left to right are as follows: a raw RGB color image, a red channel image, a green channel image, a blue channel image, the grayscale image generated from the RGB color image, and the bicolor image generated from the green and blue channels. Note that the brightness of each pixel in the images except for the raw images was expressed as  $0$ – $1023$  levels, and the colors of the images were matched to a color bar to determine fluorescence intensity. (b) Comparison of five different image analysis methods by sensor output  $\Delta I$  that was calculated by averaging a  $\Delta$ mean intensity of ROI at  $170$ – $180$  s after applying gaseous EtOH.

**2.4. Investigation of Conditions for Enzymatic Reaction (Buffer pH and NAD<sup>+</sup> Concentration).** The activity of an NAD-dependent enzyme was manipulated by varying the buffer species, pH value, and coenzyme concentration. Optimization of the reaction conditions including the buffer pH and NAD<sup>+</sup> concentration was performed in order to detect EtOH catalyzed by ADH at the highest efficiency. NAD<sup>+</sup> that was necessary for the ADH-catalyzed reaction was supplied by impregnating the ADH-immobilized mesh with an NAD<sup>+</sup> solution before conducting an experiment. The optimum conditions for this reaction were investigated by changing the buffer species, pH value, and concentration of the NAD<sup>+</sup> solution. The selection of the optimum buffer and buffer pH was carried out using the following buffers: acetic buffer (AB, at pH 3.5, 4.0, 5.0, and 6.0, using a mixture of CH<sub>3</sub>COONa and CH<sub>3</sub>COOH), PB (pH 6.0, 7.0, 7.5, and 8.0, using a mixture of Na<sub>2</sub>HPO<sub>4</sub> and KH<sub>2</sub>PO<sub>4</sub>), trisodium phosphate buffer (TPB, at pH 8.0, 9.0, 9.5, and 10.0, using a mixture of Na<sub>3</sub>PO<sub>4</sub>·12H<sub>2</sub>O and KH<sub>2</sub>PO<sub>4</sub>), Tris-HCl buffer (Tris, at pH 8.0, 8.5, 9.0, 9.5, and 10.0, using a mixture of C<sub>4</sub>H<sub>11</sub>NO<sub>3</sub> and HCl), carbonate–bicarbonate buffer (CB, at pH 9.0, 9.5, 10.0, and 11.0, using a mixture of Na<sub>2</sub>CO<sub>3</sub> and NaHCO<sub>3</sub>), sodium hydroxide buffer (SHB, pH 11.0 and 12.0, using a mixture of NaOH and Na<sub>2</sub>HPO<sub>4</sub>), and potassium chloride buffer (PCB, at pH 12.0 and 13.0, using a mixture of NaOH and KCl). All buffers were prepared at a concentration of  $0.1$  M. The ADH-immobilized mesh that was wetted with  $80$   $\mu$ L of an NAD<sup>+</sup> solution prepared using each buffer was placed in front of a camera, and then  $25$  ppm of standard gaseous EtOH was applied to the ADH-immobilized mesh. The experimental process was the same as that of the standard gas visualization experiment described in section 2.3.

The optimum concentration of NAD<sup>+</sup> was investigated using the fluorescence intensity observed from the ADH-immobilized mesh after application of  $0.005$ ,  $0.01$ ,  $0.05$ ,  $0.1$ ,  $0.5$ ,  $1$ ,  $5$ ,  $10$ ,  $50$ ,  $100$ ,  $200$ , and  $300$  ppm of gaseous EtOH with various concentrations of NAD<sup>+</sup> solutions ( $0.1$ ,  $1$ ,  $5$ ,  $10$ ,  $15$ ,  $20$ , and  $100$  mM) that were prepared by the optimum buffer solution. The absorption and fluorescence spectra of the NAD<sup>+</sup>/NADH mixture solution were measured in order to observe the effect of the initial NAD<sup>+</sup> concentration on sensor output. The NAD<sup>+</sup>/NADH solutions at various concentration ratios ( $1$ : $1$ ,

$10$ : $1$ ,  $100$ : $1$ , and  $1000$ : $1$ ) in Tris (at pH  $9.0$ ,  $0.1$  M) were prepared, and  $0.1$  mM NADH solution (in  $0.1$  M Tris, pH  $9.0$ ) was used as a control (Table S-1). The absorption and fluorescence spectra obtained at each concentration ratio of the NAD<sup>+</sup>/NADH solution were obtained on a spectrophotometer (Nanodrop 2000, Thermo Fisher Scientific) and a fluorescence spectrophotometer (F-7000, Hitachi), respectively.

**2.5. Imaging of EtOH in Breath from Healthy Subjects without the Consumption of Alcohol.** Finally, we measured the concentration distribution of breath EtOH without alcohol consumption using the improved sniff-cam. This experiment was conducted under the permission of the Human Investigations Committee of the Institute of Biomaterials and Bioengineering, Tokyo Medical and Dental University (authorization code: 2012-6). Subjects were healthy males  $24$ – $28$  years old, and we were confirmed that they do not take medicine on a daily basis. Subjects who cooperated with this experiment were forbidden to consume alcohol, take medicine, and smoke up to  $72$  h before the experiment. The exhaled breath of the subjects was applied to the ADH-immobilized mesh at a  $100$  mL/min flow rate through the breath flow rate equalizer during a  $4$  h state of fasting. The procedure used for breath gas application was the same as that used for standard gaseous EtOH.

### 3. RESULTS AND DISCUSSION

**3.1. Visualization of EtOH Based on RGB Color Images.** As shown in Supplemental Movie 1, a noticeable increase in the fluorescence intensity centered around the gas outlet on the ADH-immobilized mesh surface was observed by applying  $100$  ppm of gaseous EtOH. Figure 2a shows fluorescence images taken at  $-30$ ,  $30$ , and  $180$  s after application of gaseous EtOH. The images, from left to right, are as follows: a raw RGB color image, a red channel image, a green channel image, a blue channel image, the grayscale image generated from the RGB color image, and the bicolor image generated from the green and blue channels. Note that the brightness of the images except for the raw images was expressed as  $0$ – $1023$  levels, and the colors of the image were matched to that of a color bar in order to demonstrate the fluorescence intensity. Figure S-1 indicates the rise and plateau of the fluorescence intensity before and after application of

gaseous EtOH using the five different image-analysis methods. The rise in fluorescence intensity corresponding to the application of gaseous EtOH and the plateau corresponding to a halt in the application of gaseous EtOH were observed except for the red channel. Figure 2b shows a comparison of the sensor output  $\Delta I$  that was calculated by averaging mean intensity of ROI at 170–180 s after applying EtOH shown in Figure S-1. Fluorescence from NADH was passed through and detected only in the green and blue filters of the CMOS color filter, since the fluorescence spectrum of the NADH is in the wavelength range of 450–530 nm. The grayscale image that was calculated by eq 1 decreased in sensitivity for the fluorescence from NADH, since about 30% of the intensity in the grayscale image originates from the red channel that did not show a signal against fluorescence from NADH. On the other hand, the bicolor image demonstrated the highest sensitivity, since it used the simple addition of the green and blue channels, and they did not contain the red channel. A comparison of the background noise and S/N ratios among these imaging methods is depicted in Figure S-2. As a result, the gray method, which is the general method for analyzing RGB color images, showed the lowest background noise. The highest S/N ratio in relation to the highest output, however, was observed by using the bicolor method. Therefore, the bicolor method was used in subsequent experiments.

### 3.2. Quantitative Ability of the EtOH Sniff-Cam under Optimum Conditions. Figure 3 shows the effects of the

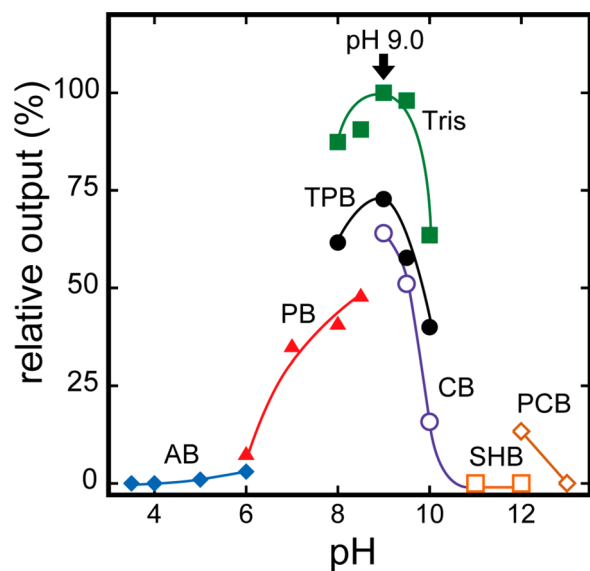


**Figure 3.** Dependence of ADH activities in response to gaseous EtOH on the buffer pH: (◆) acetic buffer, AB; (▲) phosphate buffer, PB; (●) trisodium phosphate buffer, TPB; (■) Tris-HCl buffer, Tris; (○) carbonate-bicarbonate buffer, CB; (□) sodium hydroxide buffer, SHB; (◇) potassium chloride buffer, PCB.

buffer pH on the ADH activity as indicated by the normalized output signal obtained by using Tris at a pH of 9.0. The resulting improved activity of ADH at pH 9.0 relative to that at other pH values was observed for CB, TPB, and Tris. Among these three buffers, Tris showed the most significant output. Thus, Tris at pH 9.0 was used in subsequent experiments.

Figure 4a shows the time course of mean intensity of the ROI upon application of various concentrations of EtOH (0.005, 0.01, 0.05, 0.1, 0.5, 1, 5, 10, 50, 100, 200, and 300

ppm) using typical concentrations (0.1 and 10 mM) of the NAD<sup>+</sup> solution. The relationship between the response time required to reach 90% of the mean intensity of the ROI and NAD<sup>+</sup> concentration was almost the same across all concentrations of NAD<sup>+</sup> (Figure S-3). Figure 4b shows the effect of the NAD<sup>+</sup> concentration on sensor output  $\Delta I$  (defined in Figure 2b) that was calculated from the fluorescence images obtained by applying 0.1, 1, 10, and 100 ppm of gaseous EtOH using various concentrations (0.1, 1, 5, 10, 15, 20, and 100 mM) of the NAD<sup>+</sup> solution. As a result, the highest signal was observed when 10 mM of the NAD<sup>+</sup> solution was used. It was observed that a weaker signal was induced because of an insufficient amount of NAD<sup>+</sup> at a concentration lower than 10 mM. When the initial NAD<sup>+</sup> concentration was over 10 mM, a decrease in signal occurred. Figure S-4a displays fluorescence spectra for the solutions of NAD<sup>+</sup> and NADH that were prepared as shown in Table S-1. The fluorescence intensity of the NAD<sup>+</sup>/NADH solution decreased as the NAD<sup>+</sup> concentration in the NAD<sup>+</sup>/NADH solution was increased (Figure S-4b). Additionally, Figure S-4c shows the absorbance spectra for the same solution mixtures. The absorbance at a wavelength of 340 nm increased as the NAD<sup>+</sup> concentration in the NAD<sup>+</sup>/NADH solution was increased (Figure S-4d). In general, a pure NADH solution showed a positive correlation between absorbance and fluorescence intensity. Therefore, we considered that the lower signal obtained at a higher initial concentration of the NAD<sup>+</sup> solution was caused by the inhibition of the proper excitation of NADH. This resulted from the high concentration of NAD<sup>+</sup> that absorbed UV light at a wavelength of 340 nm. Therefore, the initial concentration of NAD<sup>+</sup> was fixed at 10 mM in the subsequent experiments.

As reported in a previous study,<sup>35,36</sup> a differential analysis was performed to improve the responsiveness of the sniff-cam. The differential analysis calculated the change rate of the fluorescence intensity in each pixel of fluorescence video. First, a difference between  $I_k$  and  $I_{k-(\text{fps} \times \Delta t)}$  was determined by image subtraction, where  $I_k$  is the  $k$ th frame of fluorescence image in the video, fps is the frame rate of the video, 24, and  $\Delta t$  was 5 s. Second, the difference was divided by  $\Delta t$ . Thus, the differential value denotes amount of fluorescence change per seconds. Details of the calculations were described in previous papers.<sup>35,36</sup> As a result, changes in the differentiation of the fluorescence intensity dependent on the concentration of EtOH incident on the ADH-immobilized mesh surface were visualized, as shown in Supplemental Movie 2. Additionally, differentiation of the fluorescence intensity recovered to the baseline after stopping the application of gaseous EtOH was stopped as observed, as shown in Figure 5a. In Figure 5a, the peak maximum differentiation value is defined as  $\Delta D$ . Figure 5b displays a comparison of the dynamic ranges that were obtained by curve fitting based on  $\Delta I$  and  $\Delta D$  as shown in the following equations. Additionally, Figure S-5 indicates the dynamic ranges of this system upon using different NAD<sup>+</sup> concentrations (0.1, 1, 10, and 100 mM).

$$\Delta I = 7.93 \times [\text{EtOH}(\text{ppm})]^{0.603} \quad (3)$$

$$\Delta D = 0.167 \times [\text{EtOH}(\text{ppm})]^{0.623} \quad (4)$$

The LOQ values that were calculated by using a 10-fold standard deviation of the baseline and eqs 3 and 4 were 9.3 and 20.6 ppb for the intensity-based analysis and differential analysis, respectively. The dynamic ranges were 0.0093–300

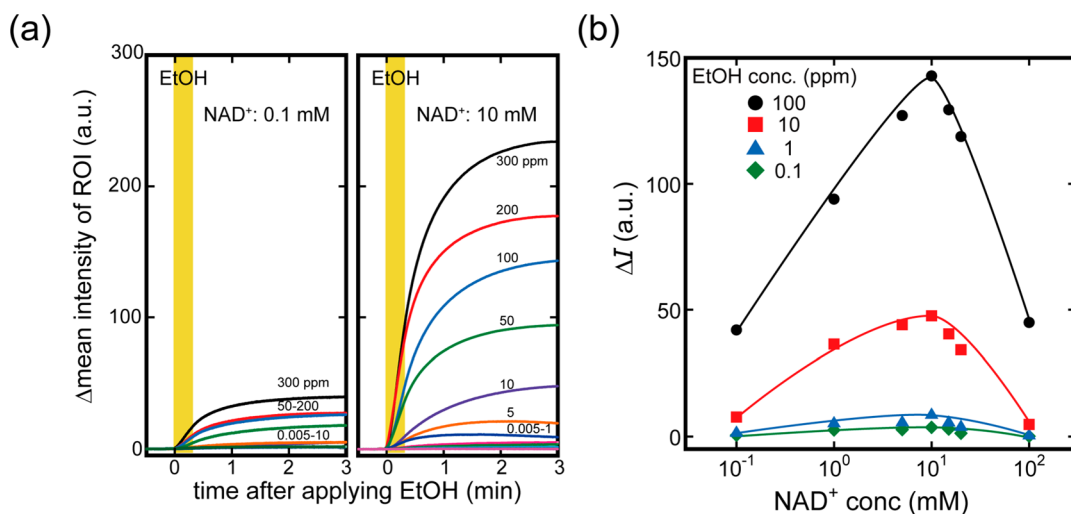


**Figure 4.** (a) Mean intensity of ROI versus time at various concentrations (0.005, 0.01, 0.05, 0.1, 0.5, 1, 5, 10, 50, 100, 200, and 300 ppm) of EtOH in 0.1 and 10 mM  $\text{NAD}^+$  solutions. (b) Effect of the initial  $\text{NAD}^+$  concentration on  $\Delta I$  that was observed by applying 0.1, 1, 10, and 100 ppm of gaseous EtOH.

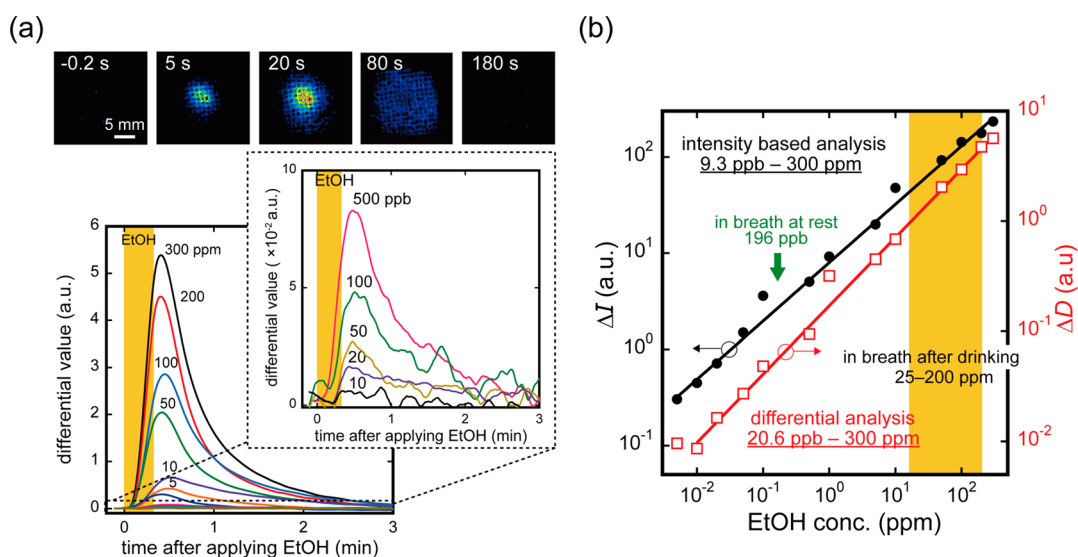


**Figure 5.** (a) Time in relation to the differential values that were calculated by differential analysis. The peak maximum value of a differential value is defined as  $\Delta D$ . (b) Comparison of the dynamic ranges that were obtained by curve fitting for  $\Delta I$  and  $\Delta D$ . LOQ values were calculated using a 10-fold standard deviation of the baseline.

and 0.0206–300 ppm, respectively. These dynamic ranges encompassed breath EtOH concentration at rest ( $196 \pm 244$  ppb)<sup>16</sup> and after alcohol consumption (25–100 ppm)<sup>35,37–39</sup> in order to visualize EtOH concentrations in breath and skin gas. Since the dynamic range of the previously reported sniff-cam was 0.5–150 ppm,<sup>35</sup> the developed system had an approximately 25-fold greater sensitivity and a broader dynamic range. The LOQ of the differential analysis was slightly worse in comparison to the intensity-based analysis. This was because  $\Delta I$  was the integrated signal of 20 s of gaseous EtOH application. In contrast, the differential analysis calculated the signal as the changing amount of fluorescence intensity within 1 s. The  $\Delta D$  value was about 10 times smaller than the  $\Delta I$  value that was obtained by the application of the same concentration of gaseous EtOH. However, the differential analysis had an advantage in sensor response in comparison to the intensity-based analysis. The 90% reaction time was improved by the differential analysis that defined the

times to reaching to  $\Delta I$  and  $\Delta D$  were about 100 and 30 s, respectively. The improvement of the sensor response would be important for monitoring of metabolism by measuring the time course of EtOH concentration in future studies. Therefore, we used the differential analysis in subsequent experiments. The Table S-2 shows a comparison of the results of the previously reported sniff-cam and the newly developed one.

**3.3. Imaging of Breath EtOH without Alcohol Consumption.** Figure S-6 displays the differential values of the fluorescence intensity over time that were obtained by applying the breath of healthy subjects during a 4 h period of fasting and without consumption of alcohol. The results indicate that the measurement of gaseous EtOH present in moist breath was possible, as was the measurement of standard gaseous EtOH. Figure 6 summarizes the breath EtOH concentration of all subjects. The concentration of breath EtOH was  $116.2 \pm 35.7$  ppb, which is almost the same as that



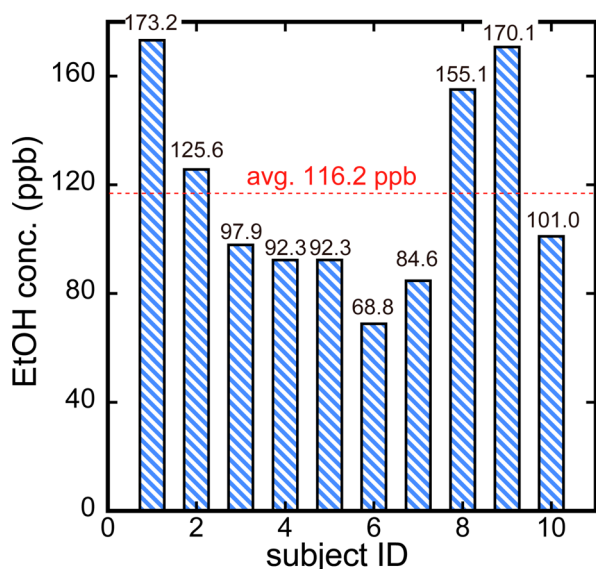


**Figure 6.** Concentrations of breath EtOH among 10 different subjects. The numbers on each bar indicate the breath EtOH concentration of each subject. The dotted horizontal line shows the average concentration of breath EtOH, which is 116.2 ppb.

of the breath EtOH concentration measured in a previous study (115 ppb) over a 2 h period during consumption of a sweet drink or meal.<sup>16</sup> The previous study used an SIFT-MS system, which is not portable; the sniff-cam used in this study, however, may be made more compact by using a smaller UV-LED and image sensor. Therefore, the sniff-cam system may be used in smartphones in the future to allow people to simply monitor their own health status.

#### 4. CONCLUSIONS

In this study, we developed an EtOH sniff-cam with improved sensitivity using a UV-LED ring light, an RGB camera, and a novel image-analysis method. First, five different image analysis methods were compared. The highest *S/N* ratio ( $>10^3$ ) for the visualization of gaseous EtOH was determined to be that of the bicolor images that were generated using green and blue channel images. Next, the buffer pH and concentration of NAD<sup>+</sup> were optimized. Finally, the quantitative characteristics of the system were investigated over a concentration range of 0.0005–300 ppm of gaseous EtOH. The results indicate that the developed system can visualize the concentration distribution of EtOH quantitatively over a wide dynamic range (0.026–300 ppm based on the differential analysis) and possesses a high correlation coefficient ( $R = 0.999$ ). This high sensitivity and dynamic range wider than that obtained with previously investigated sniff-cams suggest that the developed EtOH sniff-cam can be applied to visualize the concentration distribution of EtOH in breath in the absence of alcohol consumption. By using another NADH-dependent dehydrogenase, the visualization of gaseous EtOH and other VOCs may be achieved. Because of the versatility of this system, the sniff-cam created in this study is expected to allow a noninvasive and systematic study of the relationship among the spatiotemporal information on VOCs, diseases, and metabolism.

#### ■ ASSOCIATED CONTENT

##### Supporting Information

The Supporting Information is available free of charge on the ACS Publications website at DOI: 10.1021/acs.anal-chem.8b05840.

Numerical data to evaluate novel fluorescence imaging method, absorbance and fluorescence spectrum of NAD<sup>+</sup>/NADH mixture, effect of NAD<sup>+</sup> concentration to dynamic range of the sniff-cam, and typical responses of differentiation value with applying breath without alcohol consumption (PDF)

Video of fluorescence intensity based EtOH imaging (AVI)

Video of time-domain image differential analyzed imaging (AVI)

#### ■ AUTHOR INFORMATION

##### Corresponding Author

\*K.M.: tel, +81 3 5280 8091; fax, +81 3 5280 8094; e-mail, [m.bdi@tmd.ac.jp](mailto:m.bdi@tmd.ac.jp).

##### ORCID

Kenta Iitani: 0000-0001-5608-8863

Kohji Mitsubayashi: 0000-0002-0709-4957

##### Notes

The authors declare no competing financial interest.

#### ■ ACKNOWLEDGMENTS

This work was supported by the JSPS KAKENHI grant numbers JP19J01649, JP17H01759, JP16J09604, and JP15H04013, the Japan Science and Technology Agency (JST), and the Ministry of Education, Culture, Sports, Science and Technology (MEXT) Special Funds for “Cooperative Research Project of Research Center for Biomedical Engineering”.

#### ■ REFERENCES

- (1) Pauling, L.; Robinson, A. B.; Teranishi, R.; Cary, P. *Proc. Natl. Acad. Sci. U. S. A.* **1971**, 68 (10), 2374–2376.
- (2) Phillips, M. *Sci. Am.* **1992**, 267 (1), 74–79.
- (3) Amann, A.; Costello, B. D. L.; Miekisch, W.; Schubert, J.; Buszewski, B.; Pleil, J.; Ratcliffe, N.; Risby, T. *J. Breath Res.* **2014**, 8 (3), 034001.
- (4) de Lacy Costello, B.; Amann, A.; Al-Kateb, H.; Flynn, C.; Filipiak, W.; Khalid, T.; Osborne, D.; Ratcliffe, N. M. *J. Breath Res.* **2014**, 8 (1), 014001.
- (5) Buszewski, B.; Ulanowska, A.; Ligor, T.; Denderz, N.; Amann, A. *Biomed. Chromatogr.* **2009**, 23 (5), 551–556.
- (6) Das, M. K.; Bishwal, S. C.; Das, A.; Dabral, D.; Varshney, A.; Badireddy, V. K.; Nanda, R. *Anal. Chem.* **2014**, 86 (2), 1229–1237.
- (7) Blanchet, L.; Smolinska, A.; Baranska, A.; Tigchelaar, E.; Swertz, M.; Zhernakova, A.; Dallinga, J. W.; Wijmenga, C.; van Schooten, F. J. *J. Breath Res.* **2017**, 11 (1), 016013.
- (8) Mazzatenta, A.; Pokorski, M.; Sartucci, F.; Domenici, L.; Di Giulio, C. *Respir. Physiol. Neurobiol.* **2015**, 209, 81–84.
- (9) Bach, J.-P.; Gold, M.; Mengel, D.; Hatteshohl, A.; Lubbe, D.; Schmid, S.; Tackenberg, B.; Rieke, J.; Maddula, S.; Baumbach, J. I.; Nell, C.; Boeselt, T.; Michelis, J.; Alferink, J.; Heneka, M.; Oertel, W.; Jessen, F.; Janciauskiene, S.; Vogelmeier, C.; Dodel, R.; Koczulla, A. R. *PLoS One* **2015**, 10 (7), e0132227.
- (10) Minh, T. D. C.; Blake, D. R.; Galassetti, P. R. *Diabetes Res. Clin. Pract.* **2012**, 97 (2), 195–205.
- (11) Kwak, J.; Gallagher, M.; Ozdener, M. H.; Wysocki, C. J.; Goldsmith, B. R.; Isamah, A.; Faranda, A.; Fakharzadeh, S. S.; Herlyn,

- M.; Johnson, A. T. C.; Preti, G. J. *Chromatogr. B. Analyt. Technol. Biomed. Life Sci.* **2013**, 931 (May), 90–96.
- (12) Abaffy, T.; Möller, M. G.; Riemer, D. D.; Milikowski, C.; DeFazio, R. A. *Metabolomics* **2013**, 9 (5), 998–1008.
- (13) Schallschmidt, K.; Becker, R.; Jung, C.; Bremser, W.; Walles, T.; Neudecker, J.; Leschber, G.; Frese, S.; Nehls, I. J. *Breath Res.* **2016**, 10 (4), 046007.
- (14) Gasparri, R.; Santonico, M.; Valentini, C.; Sedda, G.; Borri, A.; Petrella, F.; Maisonneuve, P.; Pennazza, G.; D'Amico, A.; Di Natale, C.; Paolesse, R.; Spaggiari, L. J. *Breath Res.* **2016**, 10 (1), 016007.
- (15) Davies, S. J.; Španěl, P.; Smith, D. *Bioanalysis* **2014**, 6 (6), 843–857.
- (16) Turner, C.; Španěl, P.; Smith, D.; Turner, C.; Patrik, S.; Španěl, P.; Smith, D. *Rapid Commun. Mass Spectrom.* **2006**, 20 (1), 61–68.
- (17) Solga, S. F. *World J. Gastroenterol.* **2014**, 20 (27), 9017–9025.
- (18) Galassetti, P. R.; Novak, B.; Nemet, D.; Rose-Gotttron, C.; Cooper, D. M.; Meinardi, S.; Newcomb, R.; Zaldivar, F.; Blake, D. R. *Diabetes Technol. Ther.* **2005**, 7 (1), 115–123.
- (19) Minh, T. D. C.; Oliver, S. R.; Ngo, J.; Flores, R.; Midyett, J.; Meinardi, S.; Carlson, M. K.; Rowland, F. S.; Blake, D. R.; Galassetti, P. R. *Am. J. Physiol. Endocrinol. Metab.* **2011**, 300 (6), E1166–E1175.
- (20) Righettoni, M.; Schmid, A.; Amann, A.; Pratsinis, S. E. J. *Breath Res.* **2013**, 7 (3), 037110.
- (21) Xu, M.; Tang, Z.; Duan, Y.; Liu, Y. *Crit. Rev. Anal. Chem.* **2016**, 46 (4), 291–304.
- (22) Di Natale, C.; Paolesse, R.; Martinelli, E.; Capuano, R. *Anal. Chim. Acta* **2014**, 824, 1–17.
- (23) Liu, C.; Shang, L.; Yoshioka, H.-T.; Chen, B.; Hayashi, K. *Anal. Chim. Acta* **2018**, 1010, 1–10.
- (24) Shang, L.; Liu, C.; Chen, B.; Hayashi, K. *ACS sensors* **2018**, 3 (8), 1531–1538.
- (25) Turner, A. P. F. *Chem. Soc. Rev.* **2013**, 42 (8), 3184–3196.
- (26) Alam, F.; RoyChoudhury, S.; Jalal, A. H.; Umasankar, Y.; Forouzanfar, S.; Akter, N.; Bhansali, S.; Pala, N. *Biosens. Bioelectron.* **2018**, 117 (June), 818–829.
- (27) Zhang, D.; Jiang, J.; Chen, J.; Zhang, Q.; Lu, Y.; Yao, Y.; Li, S.; Logan Liu, G.; Liu, Q. *Biosens. Bioelectron.* **2015**, 70, 81–88.
- (28) Liu, L.; Zhang, D.; Zhang, Q.; Chen, X.; Xu, G.; Lu, Y.; Liu, Q. *Biosens. Bioelectron.* **2017**, 93, 94–101.
- (29) Li, S.; Zhang, D.; Liu, J.; Cheng, C.; Zhu, L.; Li, C.; Lu, Y.; Low, S. S.; Su, B.; Liu, Q. *Biosens. Bioelectron.* **2019**, 129, 284–291.
- (30) Brenet, S.; John-Herpin, A.; Gallat, F.-X.; Musnier, B.; Buhot, A.; Herrier, C.; Rousselle, T.; Livache, T.; Hou, Y. *Anal. Chem.* **2018**, 90 (16), 9879–9887.
- (31) Hurot, C.; Brenet, S.; Buhot, A.; Barou, E.; Belloir, C.; Briand, L.; Hou, Y. *Biosens. Bioelectron.* **2019**, 123, 230–236.
- (32) Ye, M.; Chien, P.-J.; Toma, K.; Arakawa, T.; Mitsubayashi, K. *Biosens. Bioelectron.* **2015**, 73, 208–213.
- (33) Chien, P.-J.; Suzuki, T.; Tsujii, M.; Ye, M.; Toma, K.; Arakawa, T.; Iwasaki, Y.; Mitsubayashi, K. *Biosens. Bioelectron.* **2017**, 91, 341–346.
- (34) Arakawa, T.; Suzuki, T.; Tsujii, M.; Iitani, K.; Chien, P.-J.; Ye, M.; Toma, K.; Iwasaki, Y.; Mitsubayashi, K. *Biosens. Bioelectron.* **2019**, 129, 245–253.
- (35) Arakawa, T.; Sato, T.; Iitani, K.; Toma, K.; Mitsubayashi, K. *Anal. Chem.* **2017**, 89 (8), 4495–4501.
- (36) Iitani, K.; Sato, T.; Naisierding, M.; Hayakawa, Y.; Toma, K.; Arakawa, T.; Mitsubayashi, K. *Anal. Chem.* **2018**, 90 (4), 2678–2685.
- (37) Wang, X.; Ando, E.; Takahashi, D.; Arakawa, T.; Kudo, H.; Saito, H.; Mitsubayashi, K. *Talanta* **2010**, 82 (3), 892–898.
- (38) Wang, X.; Ando, E.; Takahashi, D.; Arakawa, T.; Kudo, H.; Saito, H.; Mitsubayashi, K. *Analyst* **2011**, 136 (18), 3680–3685.
- (39) Arakawa, T.; Wang, X.; Kajiro, T.; Miyajima, K.; Takeuchi, S.; Kudo, H.; Yano, K.; Mitsubayashi, K. *Sensors Actuators B Chem.* **2013**, 186, 27–33.